Revealing The Degradation Mechanism of (Sr,Ca)AlSiN$_3$:Eu^{2+} Phosphor Aged Under Thermal-Moisture-Sulfur Conditions

A Combined Experimental and Ab Initio Study

Guo, Baotong; Wen, Minzhen; Tang, Hongyu; Lishik, Sergey; Fan, Xuejun; Zhang, Guoqi; Fan, Jiajie

DOI
10.1002/lpor.202300838

Publication date
2024

Document Version
Final published version

Published in
Laser and Photonics Reviews

LASER & PHOTONICS REVIEWS
www.lpr-journal.org

Revealing The Degradation Mechanism of (Sr,Ca)AlSiN$_3$:Eu^{2+} Phosphor Aged Under Thermal-Moisture-Sulfur Conditions: A Combined Experimental and Ab Initio Study

*Baotong Guo, Minzhen Wen, Hongyu Tang, Sergey Lishik, Xuejun Fan, Guoqi Zhang, and Jiajie Fan**

MAlSiN$_3$:Eu^{2+} (M = Ca, Sr) is commonly used in high-power phosphor-converted white-light-emitting diodes and laser diodes to promote their color-rendering index. However, the wide application of this phosphor is limited by the degradation of its luminescent properties in high-temperature, high-humidity, and high-sulfur-content environment. Here, the degradation mechanism of the (Sr,Ca)AlSiN$_3$:Eu^{2+} (SCASN) red phosphor under thermal-moisture-sulfur coupling conditions is investigated. Furthermore, by performing first-principles calculations, the hydrolysis mechanism on an atomic scale is assessed. The adsorption energy (E_{ads}) and charge transfer (ΔQ) results showed that H$_2$O chemically adsorbed on the (0 1 0), (3 1 0), and (0 0 1) surfaces of the CaAlSiN$_3$ (CASN) host lattice. The energy barrier for H$_2$O dissociation is only 29.73 kJ mol^{-1} on the CASN (0 1 0) surface, indicating a high dissociation probability. The formation of NH$_3$, Ca(OH)$_2$, and CaAl$_2$Si$_2$O$_8$ is confirmed by H$^+$ tended to combine with surface N atoms, while OH$^-$ combined with the surface Al/Si or Ca atoms. Moreover, ab initio molecular dynamics simulations were performed to further understand the hydrolysis process. This work offers a guidance on the design and applications of luminescent materials in LED packages with higher reliability and stability requirements in harsh environment.

1. Introduction

Traditional incandescent and fluorescent lamps are gradually being replaced due to the rapid development of high-power white light-emitting diode (wLED) technology.[1,2] In recent years, lighting requirements have gradually shifted toward energy conservation, environmental protection, health, and comfort. Therefore, next-generation wLEDs must not only be economical and highly efficient but also meet several other requirements, including health concerns, comfort, high light-color quality, low-frequency flashing, and high reliability.[3–5] Full-spectrum wLEDs with a high color-rendering index (CRI) offer great potential in indoor lighting, medical, and health lighting, plant lighting, automobiles, and other applications, making them an important development direction for solid-state lighting. LEDs utilizing phosphor materials are also known as phosphor-converted white LEDs (pc-wLEDs). Phosphor, one of the key light conversion materials, and determines the color quality of high-power pc-wLEDs, such as the luminous efficiency, CRI, correlated color temperature, and lifespan.[6] The first commercialized strategy for achieving pc-wLEDs used a combination of blue InGaN/GaN LED chips with Y$_3$Al$_5$O$_{12}$:Ce^{3+} (YAG:Ce^{3+}) yellow phosphors, which was severely challenged by a deficiency in red-light

B. Guo, M. Wen, H. Tang, J. Fan
Institute of Future Lighting, Academy for Engineering and Technology, Fudan University
Shanghai 200433, China
E-mail: jiajie_fan@fudan.edu.cn
S. Lishik
Center of LED and Optoelectronic Technologies of NAS Belarus
Minsk 220090, Belarus
X. Fan
Department of Mechanical Engineering
Lamar University
PO Box 10028, Beaumont, TX 77710, USA
G. Zhang, J. Fan
Department of Microelectronics
Delft University of Technology
Delft 2628 CD, Netherlands
J. Fan
State Key Laboratory of Applied Optics, Changchun Institute of Optics, Fine Mechanics and Physics, Chinese Academy of Sciences
Changchun 130033, China
J. Fan
Fudan Zhangjiang Institute
Shanghai 201203, China

The ORCID identification number(s) for the author(s) of this article can be found under https://doi.org/10.1002/lpor.202300838

DOI: 10.1002/lpor.202300838

components and low thermal stability.[7] One of the efficient strategies for obtaining high CRI pc-wLEDs involves the addition of red phosphors. When the temperature of pc-wLEDs is increased by the driving current of the LED chip, photoluminescence (PL) degradation, and the color-shift phenomenon will occur due to the thermal quenching properties of the phosphor, resulting in changes in emission intensity, or peak wavelength.[8] As a result, red phosphors used in next-generation high-power pc-wLEDs must be thermally and chemically stable and possess high resistance to heat and stress shock.[9–13]

Red phosphors have attracted significant attention in recent years and have been extensively studied. Nitride host $CaAlSiN_3$ activated by Eu^{2+} ions was found to be the most promising red-emitting phosphor for pc-wLED applications due to its high quantum efficiency and good thermal quenching properties.[14,15] Moreover, the emission spectrum of $CaAlSiN_3$:Eu^{2+} red phosphor can be easily regulated through the doping of alkaline earth metal ions to better satisfy practical applications.[16–18] For example, Sr^{2+} has a larger ionic radius than Ca^{2+} so that a deep-red emission shifted to shorter wavelength will be obtained when Sr^{2+} is substituted in the Ca^{2+} site of $CaAlSiN_3$:Eu^{2+} due to the weakening of the crystal field strength around Eu^{2+}. Despite of the excellent luminescent properties of $CaAlSiN_3$-based phosphors, most studies have focused on exploring new synthetic methods,[19–21] or new LED packaging forms.[22–24] However, few reports have investigated the reliability or degradation mechanism of phosphors in practical applications. Although $MAlSiN_3$:Eu^{2+} (M = Ca, Sr, and Ba) red phosphors have shown good thermal quenching properties, their PL properties will still be susceptible to humidity, resulting in poor resistance to water or moisture. Zhu et al.[25] studied the moisture-induced degradation of the (Sr,Ca)$AlSiN_3$:Eu^{2+} (SCASN) red phosphor using a high-pressure water stream test and found that the degradation of the phosphor was mainly due to the oxidation of the phosphor host and activator Eu^{2+} via an oxidation-gas penetration mechanism. Iqbal et al.[26] used a standard accelerated-aging test (85 °C & 85% RH, 1000 h) to investigate the degradation of phosphor-in-glass encapsulants with $CaAlSiN_3$:Eu^{2+} red phosphor but did not further analyze the degradation mechanism. Fan et al.[27] used a water immersion test to analyze the hydrolysis kinetics of $CaAlSiN_3$ red phosphor, and the dissolution of Ca^{2+} and OH^- caused by the hydrolysis reaction was confirmed through in situ monitored electrical conductivity and density functional theory (DFT) calculations. Additionally, LEDs are commonly contaminated with sulfur during manufacturing and operation, causing the LED components (die-attach materials and silicone/phosphor composites) to undergo vulcanization, resulting in the degradation of luminescent performance.[28,29] Therefore, it is critical to investigate the degradation mechanism of phosphors due to the presence of hazardous sulfur-containing compounds such as H_2S and SO_2.

In this study, we designed a series of long-term accelerated-aging tests to comprehensively evaluate the reliability of the SCASN red phosphor under high-temperature, high-humidity, and high-sulfur-containing environments. The degradation mechanism of the phosphor was investigated by analyzing the PL performance, microstructure (scanning electron microscopy (SEM)), chemical elements (energy-dispersive X-ray spectroscopy (EDS)), and crystalline phase (X-ray powder diffraction (XRD)). The hydrolysis procedure and mechanism were further studied at an atomic level by using first-principles calculations. This work aims to provide insights into the degradation mechanism of the SCASN red phosphor and facilitate the design of novel red phosphors or novel LED packaging with improved reliability.

2. Experimental Section

A commercialized phosphor product (Intematix R6535), consisting of the SCASN red phosphor, was selected as the sample in the long-term accelerated-aging experiments. The aging conditions were a) 100°C, b) 100°C, & 100% RH, c) 100 °C & sulfur powder (S_8), d) 100 °C & 100% RH & S_8, and e) 45° C & 85% RH & 1 ppm H_2S. The experimental processes and the equipment are shown in **Figure 1**. First, the red phosphors were placed on watch glass surfaces and separated into two separate containers with and without sulfur powder (seen in Figure 1a,c). The samples were then loaded in an oven at a constant temperature of 100 °C for 1008 h. A portion of the sample was removed every 168 h for spectroscopy and microstructure analysis. For the moisture-induced aging experiment (seen in Figure 1b), the reactions were performed in a Teflon-lined autoclave. Approximately 30 mL of water was added around the beaker, ensuring that the phosphor did not make direct contact with the water. While in the moisture-sulfur-induced aging experiment (seen in Figure 1d), the same additional sulfur powder was added to the water. Similarly, some of the samples were removed every 168 h and dried for spectroscopy and microstructure analysis. Additionally, in order to investigate the influence of corrosive gas H_2S on the SCASN phosphor, a H_2S-induced aging experiment was conducted in a gas corrosion test chamber (YAMASAKI, GH-180), which, as an attempted exploratory experiment, lasted for 2 weeks (336 h).

3. Computational Section

In this study, the hydrolysis mechanism of the SCASN phosphor was investigated based on first-principles calculations of the $CaAlSiN_3$ host lattice surface structure and the absorption behavior of H_2O on different crystal surfaces. All spin-restricted calculations (i.e., spin polarization was not considered) were performed using DFT implemented in the DMol^3 and CASTEP package.[30,31] The electronic exchange and correlation function used the generalized gradient approximation with the Perdew–Burke–Ernzerhof method.[32] The all-electron method and double numerical basis set with polarization functions (DNP) were used, and the Grimme method for DFT-D correction was adopted to describe the van der Waals interactions.[33] The Brillouin zone was sampled by a 3 × 6 × 3 Monkhorst-Pack[34] k-point mesh for both geometry optimization and electronic structure computations. The convergence criteria of the optimized structures were 2×10^{-5} Ha for energy, 4×10^{-3} Ha Å^{-1} for force, and 5×10^{-3} Å for displacement, while the convergence criterion for the self-consistent field computations was set to 1×10^{-5} Ha. The global orbital cutoff and value of smearing were set to 5.0 Å and

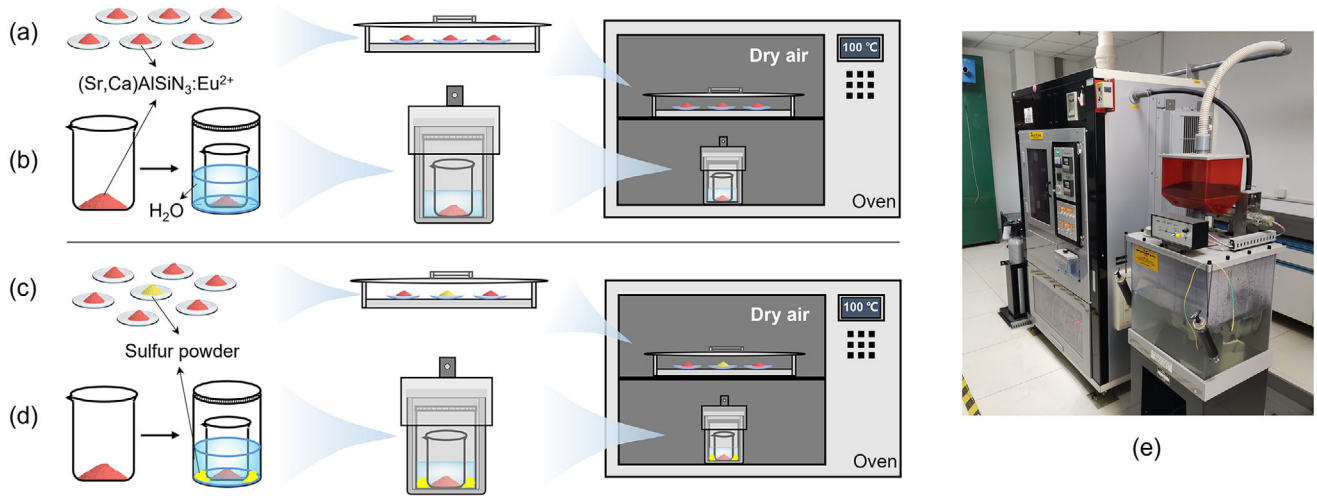

Figure 1. Schematics of the long-term accelerated-aging experiments. The aging conditions are a) 100 °C, b) 100 °C & 100% RH, c) 100 °C & S_8, d) 100 °C & 100% RH & S_8, and e) 45 °C & 85% RH & 1 ppm H_2S, respectively. e) shows the photograph of the experimental equipment (YAMASAKI, GH-180) used for the 45 °C & 85% RH & 1 ppm H_2S aging test.

5×10^{-3} Ha, respectively. The transition states were searched by the complete linear synchronous transit/quadratic synchronous transit (LST/QST) method,[35,36] which was used to study the dissociation process of the H_2O molecule on the $CaAlSiN_3$ phosphor surface.

Reports have shown that the emission spectra of $Sr_xCa_{1-x}AlSiN_3:Eu^{2+}$ red phosphor can be tuned by changing the Sr atom concentration.[15] According to crystal field theories, a blueshift will occur in the peak position due to the weaker splitting of the Eu^{2+} 5d orbital, when Sr^{2+} was substituted by Eu^{2+}, with Sr-substituted $CaAlSiN_3$ sharing the same orthorhombic crystal structure (space group 36 $Cmc2_1$) as pure $CaAlSiN_3$.[17] To simplify the model for the calculations and due to the similarity in chemical properties between alkaline earth metal Ca and Sr and the low content of activator Eu^{2+}(≈0.6%), a simplified model of $CaAlSiN_3$ was constructed, as shown in **Figure 2**. The tetrahedra of SiN_4 and AlN_4 formed six-membered rings by sharing the corner, and the rings combined into planes, forming a 3D framework. Ca^{2+} ions were distributed in the cavities of the overlaid planes, which were coordinated to five N atoms.[14] When the AlN_4/SiN_4 tetrahedron was alternately arranged in the six-membered ring, a smaller formation energy of the unit cell could be obtained, indicating that this phase was more easily crystallized.[37] The calculated parameters of the unit cell were a = 9.921 Å, b = 5.698 Å, and c = 5.077 Å, consistent with previous studies.[14,38,39]

The adsorption energy (E_{ads}) can be defined by

$$E_{ads} = E_{sub+molecule} - E_{sub} - E_{molecule} \quad \text{(i)}$$

where $E_{sub+molecule}$, E_{sub}, and $E_{molecule}$ denote the total energy of the molecule/phosphor substrate adsorption system, phosphor substrate, and the separated molecule, respectively, with a negative value of E_{ads} indicating that the molecule could stably adsorb on the substrate. The charge–transfer (ΔQ) calculated based on Milliken population analysis[40] could be defined by

$$\Delta Q = Q_{adsorpted-molecule} - Q_{isolated-molecule} \quad \text{(ii)}$$

where $Q_{adsorpted-molecule}$ and $Q_{isolated-molecule}$ represent the charge of the molecule before and after adsorption, with a negative value of ΔQ indicating electron transfer from the surface of the substrate to the adsorbing molecule. The charge density difference (CDD) could be defined by

$$\Delta\rho = \rho_{sub+molecule} - \rho_{sub} - \rho_{molecule} \quad \text{(iii)}$$

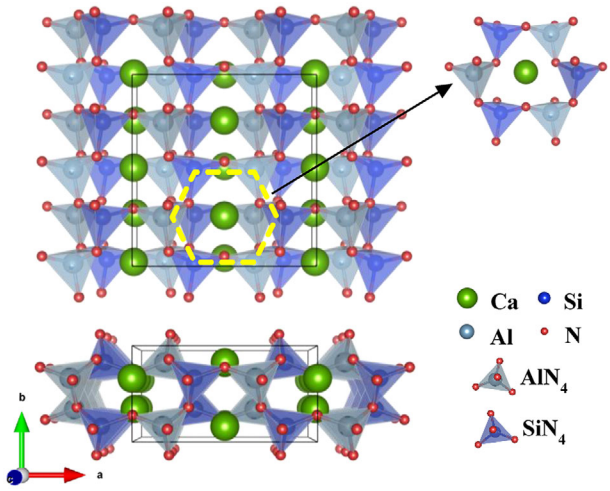

Figure 2. Top view (from c-axis) and side view (from b-axis) of the $CaAlSiN_3$ crystal structure, where the solid line shows the 1 × 1 × 2 supercell, and the yellow dashed line represents the six-membered ring consisting of AlN_4 and SiN_4.

where $\Delta\rho$, ρ_{sub}, and $\rho_{molecule}$ denote the electron density of the molecule/phosphor substrate adsorption system, phosphor substrate, and the separated molecule, respectively.

4. Results and Discussion

4.1. Experimental Results

In this section, the PL performance, micromorphology, chemical elements, and crystalline phases of the SCASN red phosphor are analyzed and its degradation mechanism is proposed.

4.1.1. Degradation of SCASN Photoluminescence Performance

The emission spectra were measured under the excitation of 475 nm blue light to evaluate the PL degradation of the SCASN red phosphor during the long-term accelerated-aging tests. As shown in **Figure 3**a,c,e, few changes were observed in the emission peaks of the samples, and PL degradation of the samples was very small under the aging conditions of a) 100 °C, c) 100 °C & S_8, and e) 45 °C, & 85% RH & 1 ppm H_2S. The color of the phosphor remains almost unchanged, which implied good thermal quenching properties and a certain degree of chemical stability of the nitride phosphors. The negligible degradation of the SCASN phosphor aged under 45 °C & 85% RH & 1 ppm H_2S probably attributed to the shorter aging time (336 h) and lower temperature and humidity. We believe that the surface hydrolysis of the phosphor under high-temperature and humidity is the most critical procedure in the phosphor degradation, these will be discussed later. Additionally, the thermal oxidation of Eu^{2+} could trigger the PL degradation of the phosphors,[13] and the slight increase in emission intensity (Figure 3f blue line) of the phosphors under the 100 °C & S_8 condition could be attributed to the reduction of Eu^{3+} by sulfur.

However, the emission spectra of the phosphors shown in Figure 3b,d, aged under the conditions of b) 100 °C & 100% RH and d) 100 °C & 100% RH & S_8, exhibited severe PL degradation, indicating that moisture was a critical factor in decreasing the PL performance of the SCASN phosphor. The peak intensity decreased, the FWHM increased, and the peak center showed a blueshift tendency over the aging time (Figure 3f,h,g). In practical applications, these will be harmful and reduce the lifetime of LEDs due to a color shift or decrease in EQE. Moreover, after the 1008 h aging test, PL performance partially disappeared under the 100 °C & 100% RH conditions, while the emission intensity of the phosphors was ≈ zero, and the phosphors were completely ineffective with a fully bleached color under the 100 °C & 100% RH & S_8 conditions. Therefore, we concluded that the presence of sulfur significantly aggravated the degradation of the SCASN:Eu^{2+} phosphor.

Gaussian peak separation was performed to further analyze the emission peak. **Figure 4**a presents the emission spectrum of the untreated SCASN phosphor under 475 nm excitation. The broad emission band was separated into two subpeaks, with peak centers at 620.0 and 656.8 nm, which corresponded to the transitions from 5d to 4f of Eu^{2+} in $SrAlSiN_3$:Eu^{2+} and $CaAlSiN_3$:Eu^{2+}, respectively. As shown in Figure 4b,c, both subpeaks gradually disappeared following the 100 °C & 100% RH & S_8 aging test. In addition, no new peak formed, indicating that the reaction products exhibited no PL performance.

4.1.2. Crystalline Phase Composition Analysis

The crystalline phase composition was analyzed using XRD, and **Figure 5** shows the XRD patterns of the SCASN phosphor aged under different conditions. After comparing with the PDF standard card, we determined that the pristine SCASN phosphor had a composition of $Sr_{0.846}Ca_{0.211}AlSiN_3$ (PDF 01-077-9188), with an expected nominal sample composition of $Sr_{0.8}Ca_{0.2}AlSiN_3$.[17] As shown in Figure 5f, the XRD pattern of the pristine SCASN phosphor coincide well with the standard data for $Sr_{0.846}Ca_{0.211}AlSiN_3$. Besides, the XRD patterns of the $CaAlSiN_3$ are shown as well. which will be discussed in the "4.2 Computational results" section. The detailed XRD patterns of the SCASN phosphors can be found in Figures S3,S4 and S5 (Supporting Information).

As shown in Figure 5a,c,f,e, minimal change was observed in the XRD patterns of the SCASN phosphor throughout the 100 °C, 100 °C, & S_8, and 45 °C & 85% RH & 1 ppm H_2S aging tests. However, the XRD patterns shown in Figure 5b presented a remarkable change under the 100 °C & 100% RH aging conditions. The peak intensity of the original crystalline phase gradually decreased with aging time, and the amorphous phase started to form at ≈504 h. After 1008 h, the aged phosphor consisted of $Sr_{0.846}Ca_{0.211}AlSiN_3$, $Sr_{0.8}Ca_{0.2}Al_2Si_2O_8$, $Ca_3(Al_2O_6)$, and $CaAl_2Si_2O_8(H_2O)_4$. Additional product phases consisting of $Sr_4(Al_6O_{12})SO_4$ and $Ca_6Al_3(OH)_{18}(SO_4)_{1.5}(H_2O)_9$ were found for the SCASN phosphor aged under the 100 °C & 100% RH & S_8 conditions. Thus, it was clear that the hydrolysis products of S_8 were also involved in the reactions of the SCASN phosphor. Moreover, the reaction products containing S element started to be detected ≈672 h according to the XRD patterns of the SCASN aged under 100 °C & 100% RH & S_8 conditions (Figure S4b, Supporting Information). The peaks of hydrolysis products, like $Ca_3(Al_2O_6)$, and $CaAl_2Si_2O_8(H_2O)_4$, got enhanced with the help of S_8, which has a stronger peak intensity and higher proportion (Figure S4b, Supporting Information) when compared with the counterparts in Figure S4a (Supporting Information). While the strongest XRD peak of SCASN decreased with a higher speed in Figure S4b (Supporting Information), indicating a higher reaction velocity. This could mean that the sulfur can promote the hydrolysis of SCASN at high-temperature and humidity by reacting with the hydrolysis products or changing the shape of phosphor particles to facilitate the contact between SCASN phosphor and water.

4.1.3. Micromorphology and Chemical Elements Analysis

The micromorphology and chemical elements were investigated using SEM and EDS analysis. As shown in **Figure 6**b,d,f, the SCASN phosphor particles still exhibited the same smooth surface and good crystallinity as the pristine particles (Figure 6a) after treatment under 100 °C or 100 °C & S_8 for 1008 h, and 45 °C & 85% RH & 1 ppm H_2S for 312 h. The particle size was also relatively uniform. These results correlated well with the analysis of the emission spectra. However, when the SCASN phosphor

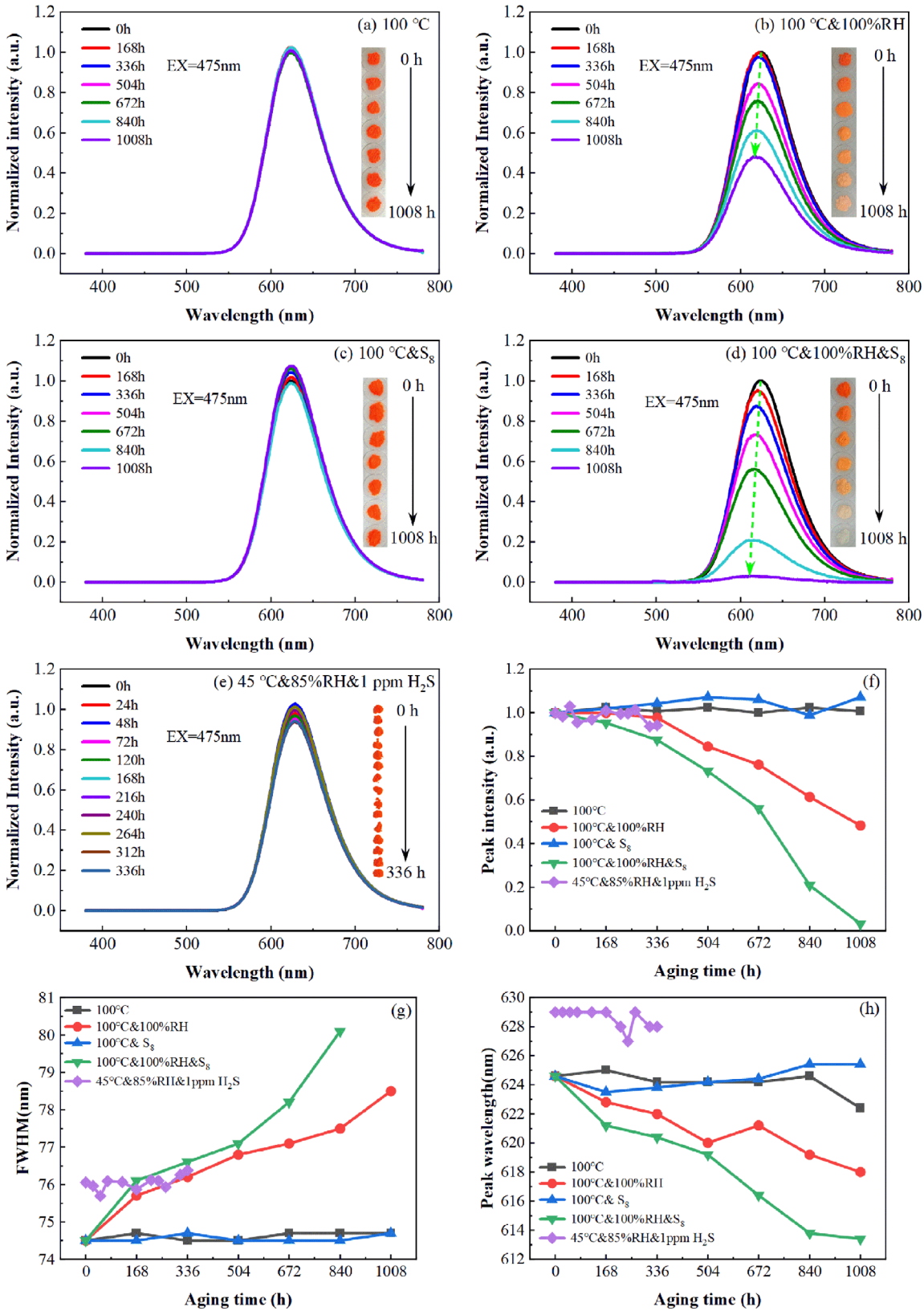

Figure 3. Emission spectra of SCASN aged under the conditions of a) 100 °C; b) 100 °C & 100% RH; c) 100 °C & S_8; d) 100 °C & 100% RH & S_8; and e) 45 °C & 85% RH & 1 ppm H_2S; changes in f) peak intensity, g) FWHM, and h) peak wavelength of the emission spectra over aging time. The inset graphics show the color changes of the SCASN phosphor.

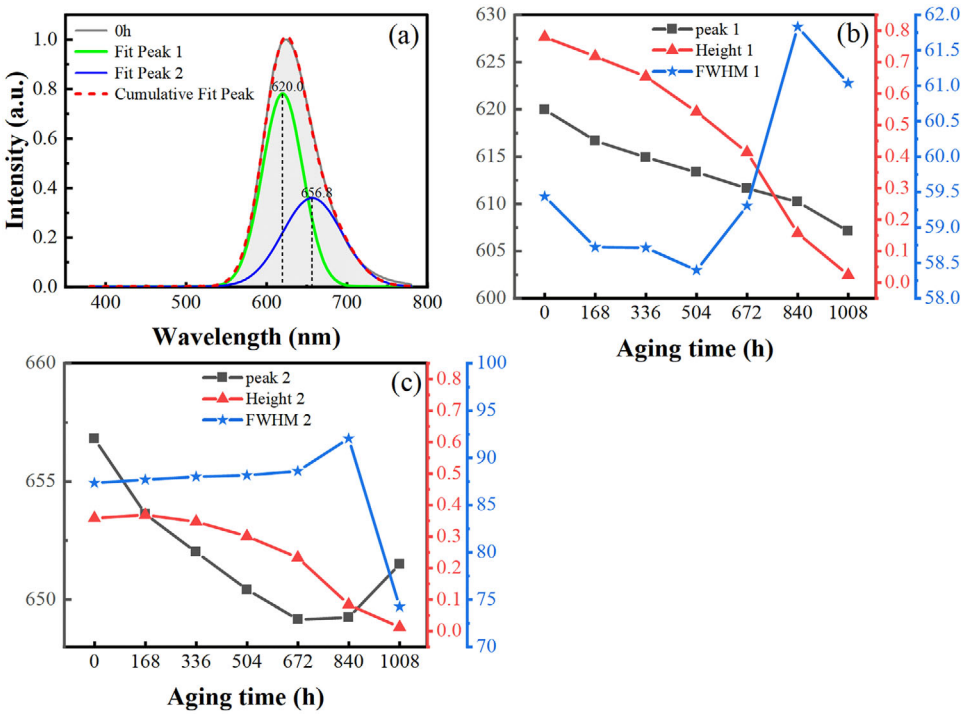

Figure 4. a) Emission spectrum of the untreated SCASN phosphor with peak separation into two subpeaks; b) and c) characteristic values of the subpeaks over time in the 100 °C & 100% RH & S_8 aging test.

was treated under 100 °C & 100% RH, the phosphor particles cracked, and their surfaces became rough due to the hydrolysis reaction[25,27] (Figure 6c). The hydrolysis procedure of the SCASN phosphor could be described as follows. First, the phosphor particles were exposed to wet environments and cracked due to surface reaction with H_2O; however, the main crystalline phase remained unchanged. Then, H_2O entered the interior of the phosphor particles through the cracks, causing the reaction rate to increase and ultimately resulting in delamination and the formation of amorphous phases. In the 100 °C & 100% RH aging test, the SCASN phosphor particles cracked but did not delaminate because the reaction temperature was not sufficiently high for SCASN to fully hydrolyze. For comparison, the SCASN phosphor particles exhibited a very irregular shape with a very rough surface, and the pristine crystalline phase entirely disappeared after the 100 °C & 100% RH & S_8 aging test.

Figure 6 (right) presents the EDS mapping images comparing the chemical element distribution of the SCASN phosphor before and after the aging tests. The chemical element distribution of the surface could be qualitatively determined, with brighter images corresponding to a greater presence of certain chemical elements. **Table 1** shows the quantitative element content results. After 100 °C or 100 °C & S_8 tests, both the metal (Ca, Sr, Eu, and Al), and Si elements remained approximately unchanged. We observed that the O element content increased to 2.62 at% in the 100 °C test and that the O and S elements increased to 6.75 at% and 0.64 at% in the 100 °C & S_8 test, respectively. This was likely due to the slight surface oxidation of the SCASN phosphor, causing it to gain weight. The oxidation of the SCASN phosphor became more significant under the 100 °C & 100% RH condition. The presence of H_2O led to the consumption of N in SCASN, releasing NH_3, which further promoted the oxidation process. Because the host lattice of SCASN was extensively oxidized, the O element content increased to 30.67 at%, and while the N element content was reduced to a very low level. In addition, the element content of the SCASN surface possibly deviated from the bulk phase, especially the N, O, and S elements. The N element content was relatively low, while the content of the O and S elements was relatively high. To some extent, this indicated that the oxidation of SCASN started at the phosphor particle surface and gradually extended inward. For the SCASN phosphor aged under the 100 °C & 100% RH & S_8 condition, the Ca and Eu elements became enriched, and the content of Sr, Al, and Si was depleted in the solid product.

4.1.4. Degradation Mechanism Analysis

The degradation of the SCASN phosphor could be primarily attributed to the hydrolysis of N atoms along with the oxidation of the host lattice. According to the analysis of the crystalline phase and chemical element, the hydrolysis reaction equations could be written as follows (Ca and Sr atoms are represented by M):

$$MAlSiN_3\,(s) + 2H_2O\,(g) \rightarrow M(OH)_2\,(s) + H_2AlSiN_3\,(s) \quad (1)$$

$$MAlSiN_3\,(s) + H_2AlSiN_3\,(s) + 8H_2O\,(g) \rightarrow MAl_2Si_2O_8\,(s) + 6NH_3\,(g) \quad (2)$$

$$2MAlSiN_3\,(s) + 10H_2O\,(g) \rightarrow MAl_2Si_2O_8\,(s) + M(OH)_2\,(s) + 6NH_3\,(g) \quad (3)$$

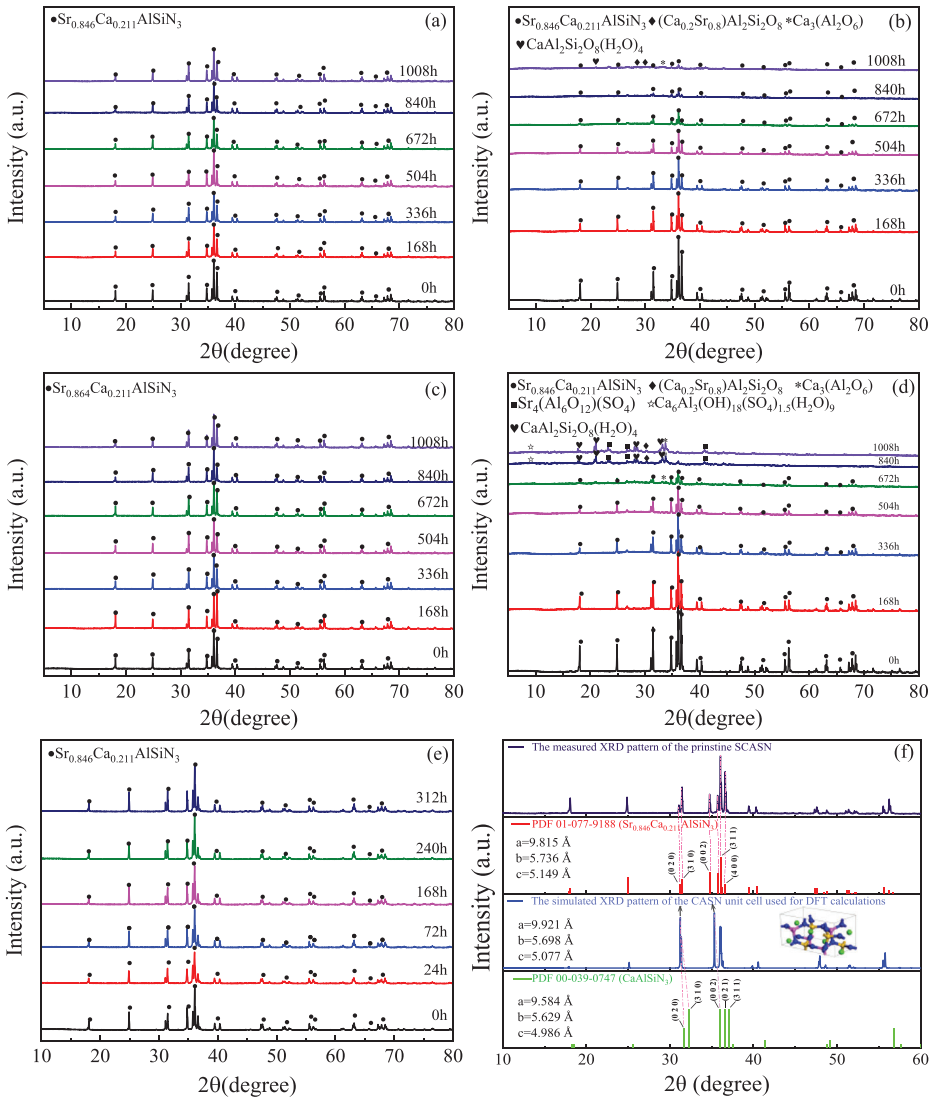

Figure 5. XRD patterns of SCASN before and after long-term aging tests: a) 100 °C; b) 100 °C & 100% RH; c) 100 °C & S_8; d) 100 °C & 100% RH & S_8; and e) 45 °C & 85% RH & 1 ppm H_2S. f) compares the XRD patterns of the pristine SCASN phosphor, standard PDF card of $CaAlSiN_3$ and the modelled $CaAlSiN_3$ unit cell that is used for the DFT calculations.

Reaction **Equation (1)** occurred on the surface of the SCASN phosphor particles, as supported by our previous work, where a rapid increase in electrical conductivity was detected in the $CaAlSiN_3$:Eu^{2+} water solution.[27] Equation (2) occurred at the interface of the H_2AlSiN_3(s) and inner $MAlSiN_3$(s). The main solid product consists of feldspar, that is, $CaAl_2Si_2O_8$ and $SrAl_2Si_2O_8$. As the gaseous NH_3 escaped from the reaction system into the air and the water vapor penetrated into the reaction interface, the reaction could continue. By combining Equation (1) and (2), the total hydrolysis reaction equation could be obtained as Equation (3). Furthermore, Equation (4) and (5) were likely involved, explaining the presence of the $Ca_3(Al_2O_6)$ crystalline phases and amorphous phases in the XRD patterns.

$$CaAl_2Si_2O_8\,(s) + 4Ca(OH)_2 \rightarrow Ca_3Al_2O_6\,(s) + 2CaSiO_3 \cdot 2H_2O\,(s) \quad (4)$$

$$CaAl_2Si_2O_8\,(s) + 4H_2O\,(g) \rightarrow CaAl_2Si_2O_8(H_2O)_4\,(s) \quad (5)$$

When exposed to sulfur-containing environments, the possible hydrolysis products of S_8, such as H_2S, SO_2, and SO_3, had to be taken into consideration. In the 100 °C & 100% RH & S_8 test, a high concentration of SO_3^{2+} was detected in the S_8 water solution. Therefore, it was reasonable to only consider the SO_2. Combined with XRD crystalline phase analysis, the following reaction equations were proposed:

$$M(OH)_2\,(s) + SO_2\,(g) + 1/2O_2\,(g) + H_2O\,(g) \rightarrow MSO_4 \cdot 2H_2O\,(s) \quad (6)$$

$$3Ca_3Al_2O_6\,(s) + 3CaSO_4 \cdot 2H_2O\,(s) + 30H_2O\,(g) \rightarrow 2Ca_6Al_3(OH)_{18}(SO_4)_{1.5}(H_2O)_9\,(s) \quad (7)$$

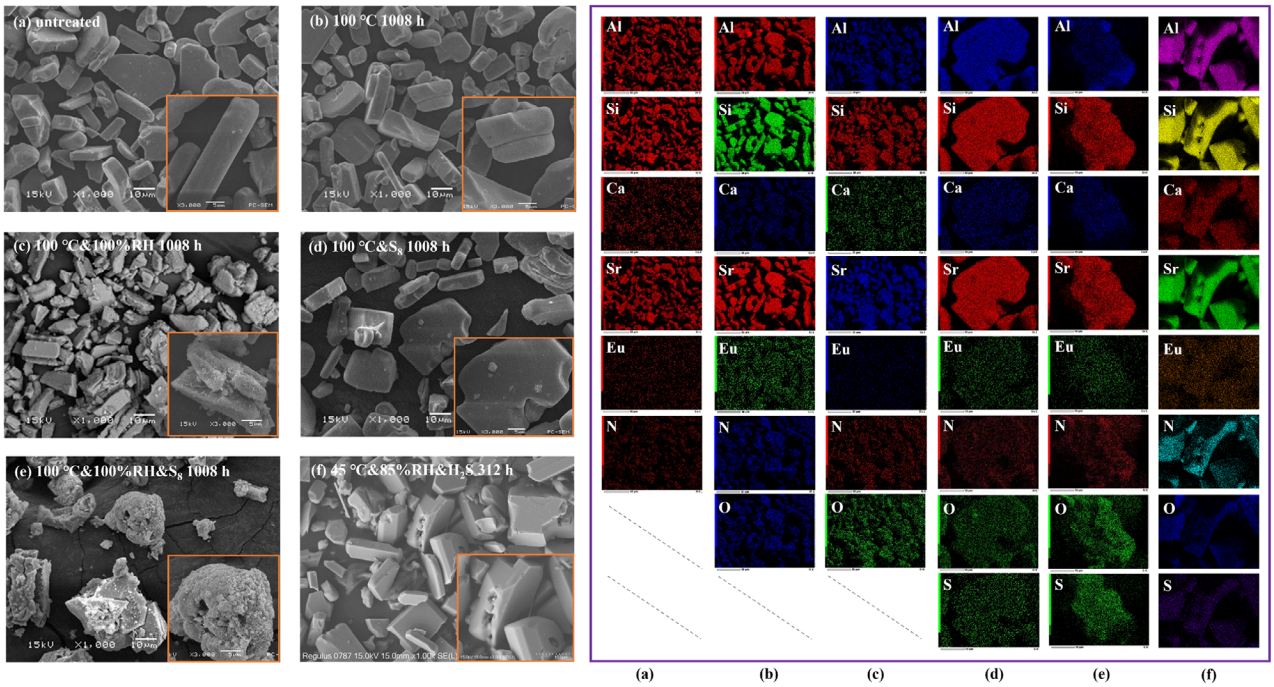

Figure 6. SEM and EDS element mapping images of the SCASN phosphor before and after aging tests: a) untreated; b) 100 °C, 1008 h; c) 100 °C & 100% RH, 1008 h; d) 100 °C & S_8, 1008 h; e) 100 °C & 100% RH & S_8, 1008 h; and f) 45 °C & 85% RH & 1 ppm H_2S, 312 h.

$$3SrAl_2Si_2O_8\,(s) + SrSO_4{\cdot}2H_2O\,(s) \rightarrow Sr_4\left(Al_6O_{12}\right)SO_4(s) + 6SiO_2\,(s) + 2H_2O\,(g) \quad (8)$$

Equation (8) converted the $SrAl_2Si_2O_8$ phase into the other phases that are determined by XRD analysis. By combining Equation (3), (4), (6), and (7), the total reaction equation of the $CaAlSiN_3$ host lattice could be obtained:

$$2CaAlSiN_3\,(s) + 11H_2O\,(g) + SO_2\,(g) + 1/2O_2\,(g) \rightarrow CaAl_2Si_2O_8\,(s) + CaSO_4{\cdot}2H_2O\,(s) + 6NH_3\,(g) \quad (9)$$

4.2. Computational Results

As the aging time increased, the XRD patterns showed a drop in peak intensity for all the crystal planes of SCASN, suggesting that hydrolysis could occur on all crystal planes. The strongest XRD peak of the SCASN correspond to SCASN (3 1 1) crystal plane with a 2θ of 36.069° (Figure 5f). Particularly, the peaks corresponding to (0 2 0), (0 0 2), and (3 1 0) crystal surfaces can also be easily distinguished from the XRD patterns of both the pristine SCASN and aged SCASN. Based on the modelled $CaAlSiN_3$ cell structure, the XRD pattern has been simulated as shown in Figure 5f. The peak positions are slightly less than the ones in the standard XRD data for $CaAlSiN_3$. It is known that the GGA functionals usually overestimates the cell parameters in DFT calculations and LDA functionals on the contrary. The cell parameters, we calculated with GGA, are a = 9.921 Å, b = 5.698 Å, and c = 5.077 Å, slightly bigger than those of the standard data for $CaAlSiN_3$ (a = 9.584 Å, b = 5.629 Å, and c = 4.986 Å) resulting in a smaller XRD peak position according to Bragg's law, $2d\sin\theta = k\lambda$. Due to the bigger radius of Sr^{2+} than Ca^{2+}, the Sr-doped $CaAlSiN_3$ has bigger cell parameters as well, with a value of a = 9.815 Å, b = 5.736 Å, and c = 5.149 Å in the case of $Sr_{0.846}Ca_{0.211}AlSiN_3$.

In our calculations, the crystal structure of SCASN has been reduced to $CaAlSiN_3$. To verify this, $CaAlSiN_3$, $SrAlSiN_3$, and

Table 1. Elemental analysis data for SCASN red phosphors before and after long-term aging tests (at%).

Aging conditions	[Ca]	[Sr]	[Eu]	[Al]	[Si]	[N]	[O]	[S]
Untreated	2.47	30.86	0.59	25.32	38.15	2.61	–	–
100 °C, 1008 h	2.64	31.02	0.63	24.29	38.80	0.07	2.62	–
100 °C&100% RH, 1008 h	2.25	21.23	0.72	17.61	27.52	<0.01	30.67	–
100 °C & S_8, 1008 h	2.60	29.62	0.61	21.97	37.81	<0.01	6.75	0.64
100 °C & 100% RH & S_8, 1008 h	7.65	19.89	2.02	9.08	21.45	<0.01	30.18	9.72
45 °C&85% RH & 1 ppm H_2S, 312 h	2.05	15.31	0.55	18.86	19.43	5.88	37.93	<0.04

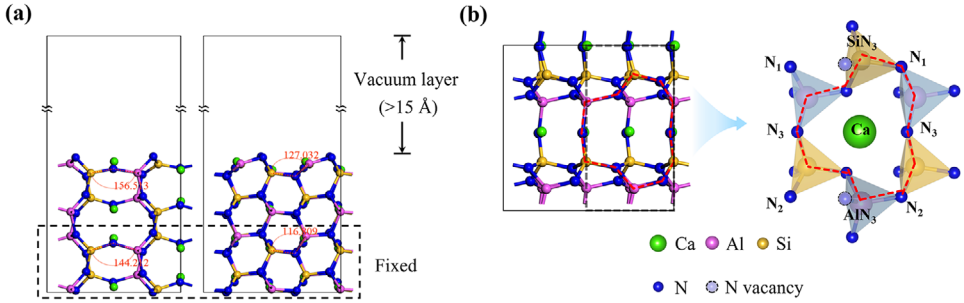

Figure 7. Optimized surface structure of $CaAlSiN_3$ (0 1 0) from the a) x, y-axis and b) z-axis, with the adsorption sites also shown in b). In the figure, the unit cell is represented by the black dashed line, and the red dashed line indicates the six-membered ring of the SiN_4 and AlN_4 tetrahedra with N vacancies.

$SrCaAlSiN_3$ unit cells were built. By carrying out geometry optimizations of the H_2O/substrate system, we find that optimized structures are almost same in spite of the difference in Sr or Ca. Figure S6 (Supporting Information) compares the calculated structures of $H_2O/CaAlSiN_3$, $H_2O/SrAlSiN_3$, and $H_2O/SrCaAlSiN_3$. Considering the (0 2 0), (0 0 2), and (3 1 0) crystal planes have stronger peak intensity in the simulated XRD pattern and easy to build surface slab models, the $CaAlSiN_3$ (0 1 0), (0 0 1), and (3 1 0) surfaces were studied in this work to reveal the degradation mechanisms of the $CaAlSiN_3$-based phosphors.

4.2.1. Adsorption of H_2O On the $CaAlSiN_3$ (0 1 0) Surface

The adsorption behavior of H_2O on the $CaAlSiN_3$ (0 1 0) surface was studied in detail, which provided insight into the hydrolysis mechanism of the SCASN red phosphor. Slab surface models were adopted, where the thickness of the vacuum layer was at least 15 Å to avoid interactions between the adjacent layers. To simulate the bulk phase, the coordinates of the lower half of the atoms were fixed. **Figure** 7 presents the fully relaxed $CaAlSiN_3$ (0 1 0) surface, exhibiting a slight shift in surface atomic coordinates and an increase in Si—N—Al bond angles. As shown in Figure 7b, three kinds of unsaturated N atoms (outermost N_1, N_2, and second layer N_3) were present when crystal symmetry was considered. The unsaturated N_3 atoms were originally present in the bulk $CaAlSiN_3$ structure with a proportion of one-third.[14] Furthermore, due to N vacancies, the coordination number (CN) of some Si/Al atoms decreased, and creating possible adsorption sites for molecules such as H_2O, H_2S, and O_2.

The AlN_3-, SiN_3-, and Ca-sites were considered in the calculations of H_2O adsorption. Several different postures of H_2O molecule were taken into account. All the initial configurations and optimized structures can be found in Figure S2 (Supporting Information). **Table** 2 shows the results of adsorption energy (E_{ads}), charge–transfer (ΔQ) and distances of different atoms. By analysing E_{ads}, ΔQ and the changes of H_2O before and after adsorption, we can conclude that there are three adsorption forms of H_2O on the surface of $CaAlSiN_3$ (0 1 0), that is, chemical adsorption on AlN_3/SiN_3 sites (No.1,2), electrostatic adsorption (No.3,4), and hydrogen bond adsorption (No.5–10) on Ca sites, as shown in **Figure** 8. The adsorption configurations of these three adsorbing forms are shown in **Figure** 9a.

When chemically adsorbed on AlN_3 (SiN_3) site, the H_2O molecule dissociated into H^+ and OH^-, and then H^+ combined with the surface N atom with an adsorption distance of 1.026 Å (1.025 Å), while OH^- combined with the Al (Si) atom with an adsorption distance of 1.824 Å (1.731 Å). Additionally, the value of E_{ads} was −3.273 eV for adsorption on AlN_3 and −2.686 eV for adsorption on SiN_3, while ΔQ was −0.372 *e* for adsorption on AlN_3 and −0.299 *e* for adsorption on SiN_3. These values were significantly higher than the other two adsorption methods,

Table 2. Adsorption energy (E_{ads}), charge–transfer (ΔQ) and the distance between different atoms of H_2O adsorption on the $CaAlSiN_3$ (0 1 0) surface.

Number	Configurations		Distance [Å]			E_{ads} [eV]	ΔQ [*e*]	Angle (°)	Length [Å]	
			H-N$^{(i)}$ (i = 1, 2, and 3)		Al/Si-O	Ca-O			∠H-O-H	O-H	
#1	AlN_3-site		1.026$^{(2)}$		1.824	2.734	−3.273	−0.372	–	0.971	
#2	SiN_3-site		1.025$^{(1)}$		1.731	3.335	−2.686	−0.299	–	0.972	
#3	Ca-site	p-up_L-R	–	–	–	2.424	−0.784	0.035	106.125	0.970	0.971
#4		p-down_L-R	–	–	–	2.404	−0.792	0.035	106.026	0.973	0.976
#5	Ca-site	p-up_l-O	1.923$^{(3)}$	1.959$^{(1)}$	–	2.419	−1.397	−0.084	97.971	1.008	1.002
#6		p-down_l-O	2.147$^{(3)}$	1.874$^{(1)}$	–	2.434	−1.391	−0.077	98.710	0.992	0.101
#7		p-left_H	1.746$^{(3)}$	2.374$^{(2)}$	–	2.442	−1.427	−0.099	97.502	1.036	0.985
#8		p-left_V	1.742$^{(3)}$	2.375$^{(2)}$	–	2.436	−1.427	−0.101	97.609	1.038	0.985
#9		p-right_H	1.978$^{(3)}$	1.918$^{(1)}$	–	2.428	−1.399	−0.083	98.016	1.002	1.005
#10		p-right_V	1.921$^{(3)}$	1.960$^{(1)}$	–	2.426	−1.396	−0.084	98.016	1.007	1.002

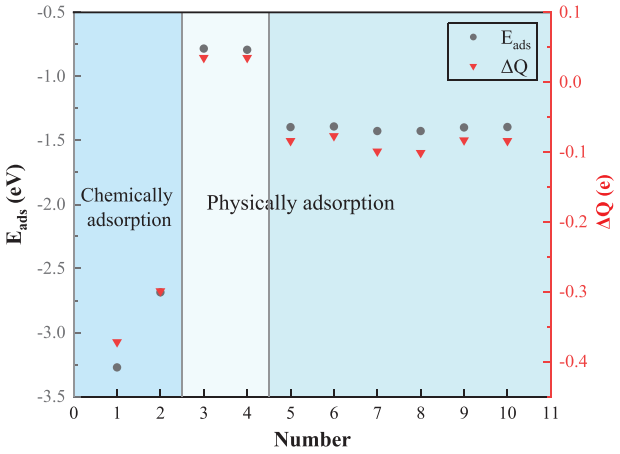

Figure 8. Graph of the adsorption energy (E_{ads}) and charge–transfer (ΔQ) for the different configurations of H_2O adsorption on the $CaAlSiN_3$ (0 1 0).

indicating stronger interactions between H_2O and the $CaAlSiN_3$ (0 1 0) surface. Moreover, when H_2O was physically adsorbed via hydrogen bonds or electrostatic interactions, the bond angle of ∠H—O—H and bond length of O—H were almost unchanged (the counterparts were 103.609° and 0.971 Å in the free H_2O molecule). Approximately 0.035 *e* of charge was transferred from H_2O to the substrate when H_2O adsorbed on the top of the Ca atom via electrostatic interactions.

The chemical bonds and vdW interactions were analyzed using the CDD and electron localization function (ELF). Figure 9b presents the CDD plots of H_2O on $CaAlSiN_3$ (0 1 0). The charge mainly accumulated around the O atoms, and the depletion of charges mainly occurred around the H atoms as well as the vacuum regions between O and Ca or between O and Al/Si atoms. Ionized H^+ and OH^- combined with the N and Al/Si atoms, respectively, and a large charge redistribution was observed, indicating strong interactions between the atoms. The ELF plots are presented in Figure 9c, showing that the ELF value between H and N was close to 0.50 (AlN_3- and SiN_3-sites), which indicated that the electrons were fully delocalized, and further demonstrated covalent bonding between the atoms. By contrast, the charge density redistribution was small and the ELF plot did not overlap when H_2O adsorbed on the Ca-sites, implying vdW interactions (hydrogen bonds) between the H and N and electrostatic interactions (ionic bonds) between Ca and O. Therefore, the H_2O molecule was physically adsorbed by a single Ca—O bond and two hydrogen bonds (O—H—N) with a Ca—O bond.

Because the H_2O molecules could be strongly adsorbed by chemical bonds or weakly adsorbed by vdW interactions, investigations into H_2O dissociation were beneficial for determining the kinetic procedure of hydrolysis. As shown in **Figure 10**, the transition state of H_2O dissociation was obtained by transient state (TS) search, where a small value of energy barrier of 29.73 kJ mol^{-1} indicates that H_2O could easily dissociate with the help of unsaturated tetrahedron of AlN_4 or SiN_4 on the $CaAlSiN_3$ (0 1 0) surface.

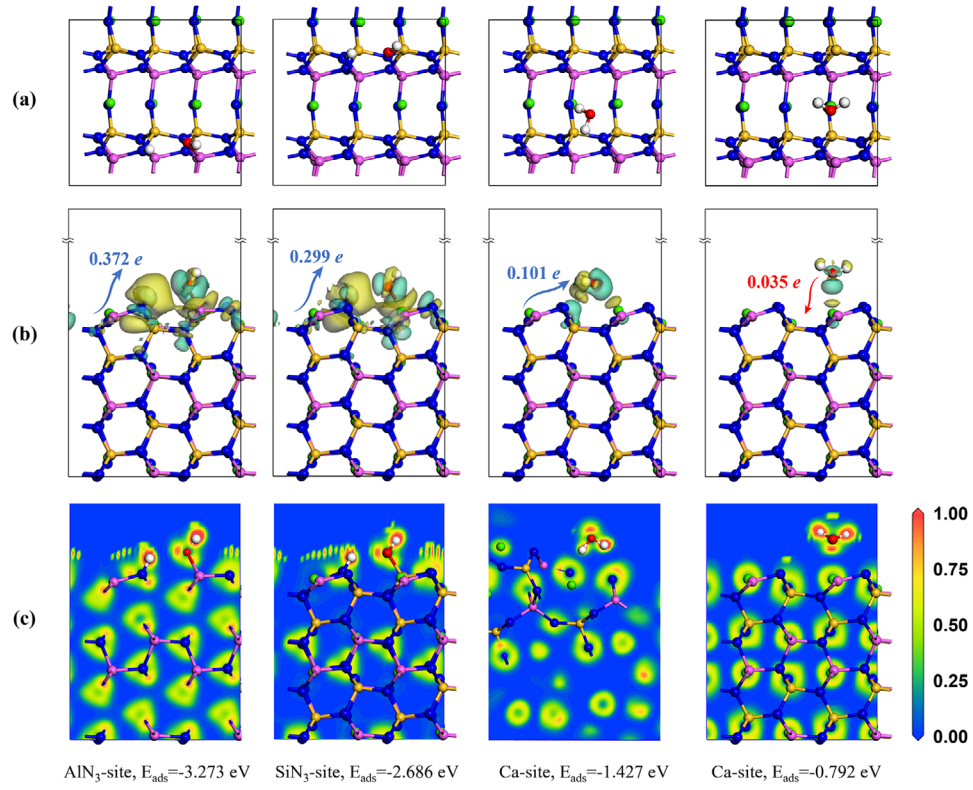

Figure 9. a) Stable configurations, b) charge density difference (CDD) plots, and c) electron localization function (ELF) of H_2O adsorption on the $CaAlSiN_3$ (0 1 0) surface AlN_3-site, SiN_3-site, and Ca-site, with an isosurface value of 0.02 e $Å.^{-3}$ The cyan region indicates charge accumulation, and the yellow region represents charge depletion, with the value ELF in the range of 0.00–1.00. In addition, ELF = 0.00 represents a very low charge density, while ELF = 0.50 and 1.00 indicate fully delocalized electrons and fully localized electrons, respectively.

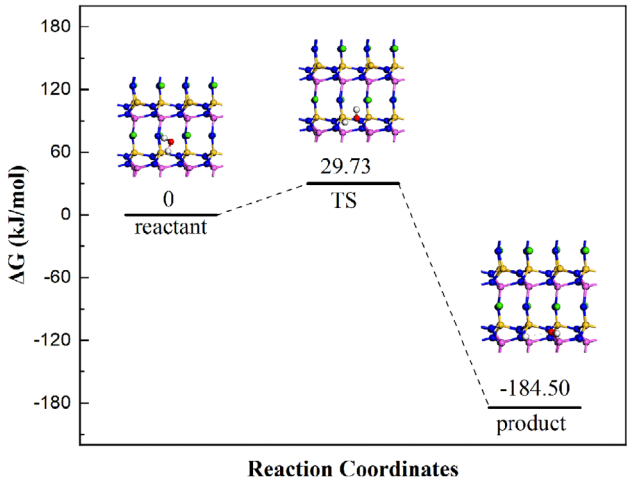

Figure 10. Minimum-energy pathway of H_2O dissociated on the $CaAlSiN_3$ (0 1 0) surface.

4.2.2. Adsorption of H_2O On the $CaAlSiN_3$ (0 0 1) and (3 1 0) Surface

To further understand the hydrolysis mechanism of the $CaAlSiN_3$ host lattice, the adsorption behaviors of H_2O on the $CaAlSiN_3$ (0 0 1) and (3 1 0) surfaces were analyzed. **Table 3** lists the E_{ads} and ΔQ results, as well as the distances between the atoms and structural parameters of the H_2O molecule. As shown in **Figure 11**, the surface contained unsaturated Al (CN = 3), Si (CN = 3), and N (CN = 2) atoms, which served as possible H_2O adsorption sites. As shown in Figure 11a,b,c, the H_2O molecule could also dissociate into H^+ and OH^- on the CASN (3 1 0) surface. H^+ combined with the nearest N atom while OH^- combined with the Al atom or Ca^{2+}, indicating the formation of NH_3 or $Ca(OH)_2$. Furthermore, the H_2O molecule could be adsorbed on top of the Si atom as an electron donator, and the charge–transfer was 0.107 *e* from H_2O to the CASN (3 1 0) substrate. As shown in Figure 11d,e,f, all Al and Si atoms in the first layer atoms of the CASN (0 0 1) surface were unsaturated. After dissociation of the H_2O molecule, OH^- was combined with the Al atom, while H^+ combined with the Si atom with an adsorption distance of 1.505 Å for the dangling bond of Si, as verified by the ELF plots shown in Figure 11f. Additionally, a metastable H_2O adsorption configuration was obtained, and the H_2O molecule adsorbed via a Ca—O bond (2.301 Å) and Si—H bond (1.971 Å). Due to the symmetrical atom distribution around H_2O, this configuration was relatively stable. A negative activation energy was also obtained by performing the TS search, indicating that the structure could be converted more easily.

4.2.3. Ab Initio Molecular Dynamics Simulation Of Hydrolysis Of the CASN Host Lattice

According to the experimental studies, the hydrolysis of the host lattice dominated the degradation of the SCASN phosphor. Therefore, ab initio molecular dynamics (AIMD) simulations were performed using DMol[3] to reveal the H_2O adsorption and NH_3 conformation mechanisms. The Massive GGM thermostat was adopted, and the model used for calculation consisted of the CASN (3 1 0) surface with a total number of eight H_2O molecules. The 0.5 ps AIMD trajectory was generated by the NVT ensemble at 373 K with a time step of 1 fs, as shown in **Figure 12**. The initial hydrolysis progress mainly consisted of two stages. The first stage occurred within 100 fs, corresponding to the relaxation progress of the CASN (3 1 0) surface, and the H_2O molecules approached the surface. In the second stage, the dissociation of H_2O occurred, accompanied by the adsorption of H^+ and OH^-. The surface coverage (θ) was defined as the ratio of adsorbed adsorbates to the adsorption sites. Four N sites were present for H^+ in the model, along with four Al/Si sites for OH^-. After an AIMD simulation time of 0.5 ps, the coverage values of H^+ (θ_1) and OH^-/H_2O (θ_2) were 75% and 50%, respectively, as shown in Figure 12b.

To compare the influence of temperature, a 4 ps AIMD trajectory was generated in the NVT ensemble at 473 K with a time step of 2 fs, as shown in **Figure 13**. A time of 0.25 ps was required to reach 75% θ_1 in the 473 K simulation, which was shorter than that in the 373 K simulation (0.35 ps). As shown in Figure 13b, the surface coverage of H^+ and OH^-/H_2O gradually increased before 0.874 ps and then became stable. The maximum of θ_1 reached 125%, indicating that some of the N atoms combined with at least two H atoms, as shown in Figure 13c. Therefore, we inferred that NH_3 would form when N-Al degraded due to the crystalline defects or energy disturbance of the system.

Table 3. Adsorption energy (E_{ads}), charge–transfer (ΔQ), and distance between the different atoms for H_2O adsorption on the $CaAlSiN_3$ (3 1 0) and (0 0 1) surfaces.

Surface	Adsorption site	Distance [Å]				E_{ads} [eV]	ΔQ [*e*]	Angle (°)	Length [Å]	
		N-H	Si-H	Al/Si-O	Ca-O			H-O-H	O-H	
(3 1 0)	Al-top	1.026	–	1.801	–	−4.792	−0.369	–	0.992	
	Si-top	2.274	–	1.973	–	−1.381	0.107	106.584	0.983	0.994
	Ca-top	1.027	–	1.832	2.417	−4.157	−0.366	–	0.971	
(0 0 1)	Al-top	–	1.505	1.797	–	−4.852	−0.948	–	0.971	
	Si-top	–	1.505	1.815	–	−4.455	−0.852	–	0.965	
	Ca-top	–	1.971	–	2.301	−1.442	−0.316	108.267	0.971	1.130

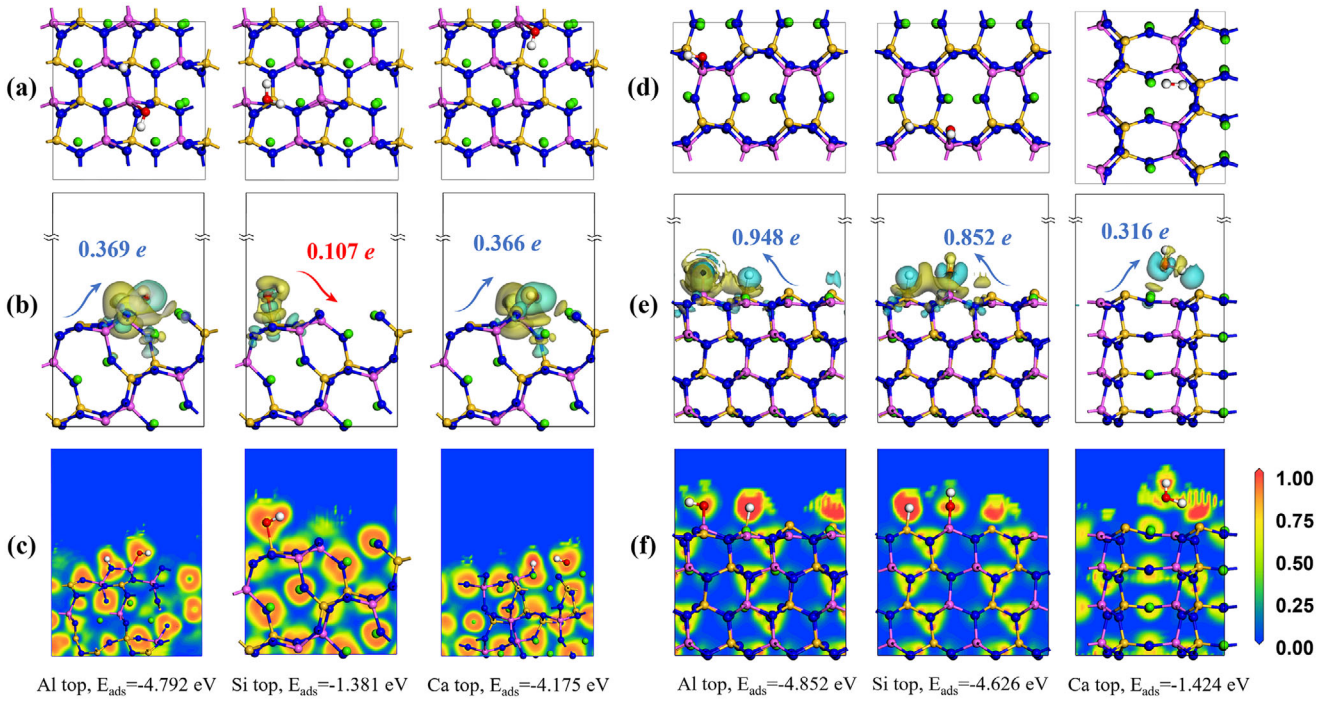

Figure 11. a), d) Stable configurations; b), e) charge density difference (CDD) plots; and c), f) electron localization function (ELF) of H_2O adsorption on the $CaAlSiN_3$ (3 1 0) and (0 0 1) surfaces (Al-top, Si-top, and Ca-top).

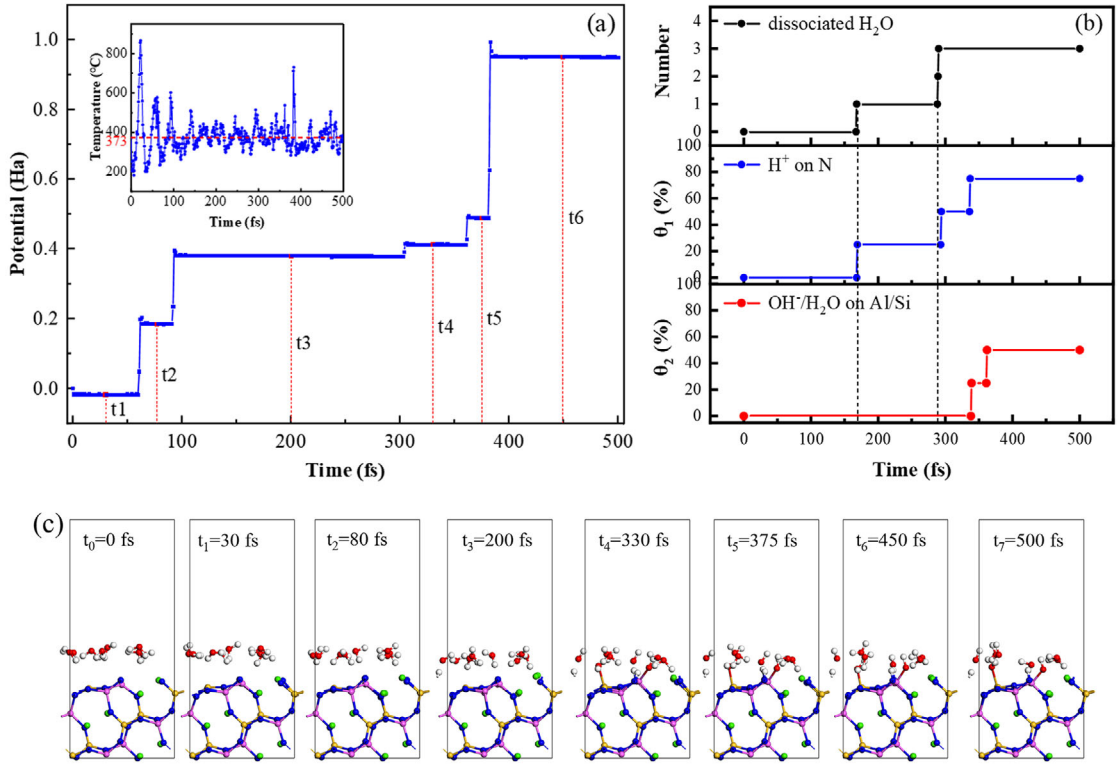

Figure 12. AIMD simulation with a temperature of 373 K (100 °C) for CASN hydrolysis; a) potential energy, b) surface coverage, and c) configurations at certain times. The inset graph shows the temperature of the system, with the potential energy of the initial structure set to zero.

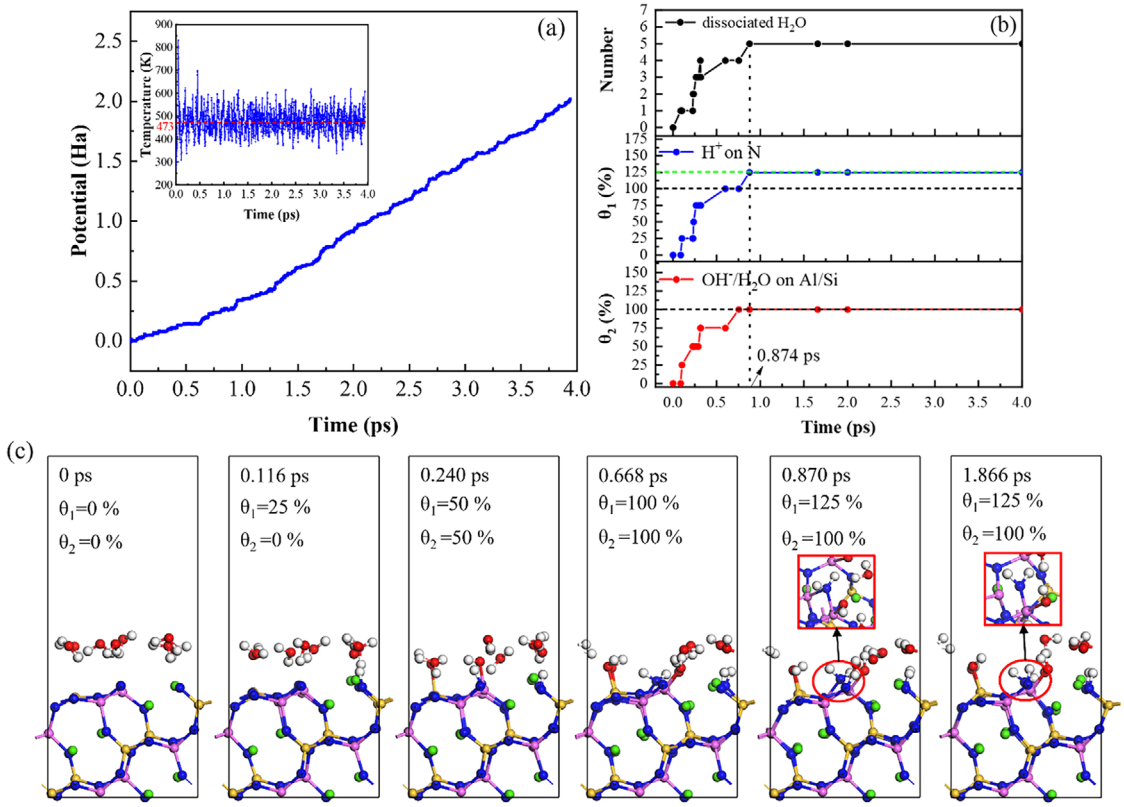

Figure 13. AIMD simulation with a temperature of 473 K (200 °C) for CASN hydrolysis; a) potential energy, b) surface coverage, and c) configurations at certain times.

5. Conclusion

The degradation mechanism of the SCASN red phosphor was studied using accelerated-aging tests and DFT calculations. This work may benefit the design of LED packages with higher reliability and the development of novel phosphors with higher stability. First, aging tests under the conditions of 100 and 100 °C & S_8 with dry air were used to verify the thermal and chemical stability. The thermal-moisture-sulfur coupling aging tests showed that the SCASN phosphor exhibited poor resistance to moisture, and significant degradation of the PL properties was observed. According to the analysis of the microstructure, element contents, and crystalline phase, the mechanism of degradation, induced by the surface hydrolysis, was proposed. The surfaces of the SCASN phosphor particles readily underwent hydrolysis resulting in the release of gaseous NH_3, the dissolution of Ca^{2+}/Sr^{2+}, and the degradation of the crystal structure. As the hydrolysis reaction interface moved inward, the phosphor cracked, and which promoted the hydrolysis process due to the increased surface area. According to XRD analysis, the solid hydrolysis products mainly consisted of $Sr_{0.8}Ca_{0.2}Al_2Si_2O_8$, $Ca_3(Al_2O_6)$, and $CaAl_2Si_2O_8(H_2O)_4$. In the environments with sulfur, these products further transformed to $Sr_4(Al_6O_{12})SO_4$, $Ca_6Al_3(OH)_{18}(SO_4)_{1.5}(H_2O)_9$, and $CaAl_2Si_2O_8(H_2O)_4$, which aggravated the hydrolysis process. First-principles calculations were conducted to assess the adsorption behavior of H_2O molecules on the different CASN crystal surfaces, which further revealed the hydrolysis mechanism from an atomic perspective. The adsorption energy (E_{ads}) and charge–transfer (ΔQ) results showed that H_2O could chemically adsorb on the CASN (0 1 0), (3 1 0), or (0 0 1) surfaces. The energy barrier for H_2O dissociation was only 29.73 kJ mol^{-1} on the CASN (0 1 0) surface, indicating a high dissociation probability. This suggested the formation of NH_3, $Ca(OH)_2$, and $CaAl_2Si_2O_8$ was verified by that H^+ tended to combine with surface N atoms and OH^- tended to combine with the surface Al/Si or Ca atoms. By performing AIMD simulations of CASN (3 1 0) surface hydrolysis, we could study the effects of temperature and surface coverage of H^+ with a value of >100%, which further indicated NH_3 formation.

Supporting Information

Supporting Information is available from the Wiley Online Library or from the author.

Acknowledgements

The work described in this paper was partially supported by the National Natural Science Foundation of China (52275559, 51805147), the State Key Laboratory of Applied Optics (SKLAO2022001A01), the Shanghai Science and Technology Development Foundation (21DZ2205200) and the Shanghai Pujiang Program (2021PJD002).

Correction added on 5 February 2024, after first online publication: Formatting errors have been updated in this version.

Conflict of Interest

The authors declare no conflict of interest.

Data Availability Statement

The data that support the findings of this study are available on request from the corresponding author. The data are not publicly available due to privacy or ethical restrictions.

Keywords

(Sr, Ca)$AlSiN_3$:Eu^{2+} phosphor, degradation mechanism, first-principles calculation, hydrolysis reaction, sulfur and hydrogen sulfide

Received: August 30, 2023
Revised: January 15, 2024
Published online: January 31, 2024

[1] Z. Y. Liu, S. Liu, K. Wang, X. B. Luo, *IEEE Photonics Technol. Lett.* **2008**, *20*, 2027.
[2] S. Pimputkar, J. S. Speck, S. P. DenBaars, S. Nakamura, *Nat. Photonics* **2009**, *3*, 180.
[3] J. J. Fan, K. C. Yung, M. Pecht, *IEEE Trans. Device Mater. Reliab.* **2014**, *14*, 564.
[4] J. Fan, M. G. Mohamed, C. Qian, X. Fan, G. Zhang, M. Pecht, *Materials* **2017**, *10*, 819.
[5] M. Cai, D. Yang, J. Huang, M. Zhang, X. Chen, C. Liang, S. Koh, G. Zhang, *IEEE Photonics J.* **2017**, *9*, 8200114.
[6] C. C. Lin, R. S. Liu, *J. Phys. Chem. Lett.* **2011**, *2*, 1268.
[7] J. Ueda, P. Dorenbos, A. J. J. Bos, A. Meijerink, S. Tanabe, *J. Phys. Chem. C* **2015**, *119*, 25003.
[8] Y. H. Kim, N. S. M. Viswanath, S. Unithrattil, H. J. Kim, W. B. Im, *ECS J. Solid State Sci. Technol.* **2017**, *7*, R3134.
[9] J. J. Fan, M. N. Zhang, X. Luo, C. Qian, X. J. Fan, A. M. Ji, G. Q. Zhang, *J. Mater. Sci.: Mater. Electron.* **2017**, *28*, 17557.
[10] S. Y. Hui, S. N. Li, X. H. Tao, W. Chen, W. M. Ng, *IEEE Trans. Power Electron.* **2010**, *25*, 2665.
[11] E. F. Schubert, J. K. Kim, *Science* **2005**, *308*, 1274.
[12] P. Singh, C. M. Tan, *Sci. Rep.* **2016**, *6*, 24052.
[13] Z. H. Ma, H. C. Cao, X. J. Sun, C. Yang, X. Xi, J. Li, S. Lin, L. X. Zhao, *Phys. Status Solidi A* **2019**, *216*, 1800335.
[14] K. Uheda, N. Hirosaki, Y. Yamamoto, A. Naito, T. Nakajima, H. Yamamoto, *Electrochem. Solid-State Lett.* **2006**, *9*, H22.
[15] R.-J. Xie, N. Hirosaki, *Top. Appl. Phys.* **2013**, *126*, 291.
[16] Y. Q. Li, J. E. J. van Steen, J. W. H. van Krevel, G. Botty, A. C. A. Delsing, F. J. DiSalvo, G. de With, H. T. Hintzen, *J. Alloys Compd.* **2006**, *417*, 273.
[17] H. Watanabe, N. Kijima, *J. Alloys Compd.* **2009**, *475*, 434.
[18] K. Zhu, Z. Chen, Y. Wang, H. Liu, Y. Niu, X. Yi, Y. Wang, X. Yuan, G. Liu, *J. Lumin.* **2022**, *252*, 119288.
[19] W. W. Hu, C. Cai, Q. Q. Zhu, X. Xu, L. Y. Hao, S. Agathopoulos, *J. Alloys Compd.* **2014**, *613*, 226.
[20] G. Li, Y. Zhao, J. Xu, Z. Mao, J. Chen, D. Wang, *Mater. Chem. Phys.* **2017**, *201*, 1.
[21] J. J. Shyu, C. H. Wu, *Int. J. Appl. Ceram. Technol.* **2023**, *20*, 3163.
[22] C. C. Huang, T. H. Weng, C. L. Lin, Y. K. Su, *Coatings* **2021**, *11*, 239.
[23] R. Wang, M. Y. Wang, G. Li, J. H. Zhang, Y. J. Zhang, H. Lin, E. Y. B. Pun, D. S. Li, *J. Lumin.* **2020**, *225*, 117390.
[24] X. W. Zhang, J. X. Liu, J. L. Liu, Y. Peng, J. J. Li, T. L. Shi, *IEEE Trans. Electron Devices* **2021**, *68*, 4473.
[25] J. Zhu, L. Wang, T. L. Zhou, Y. J. Cho, T. Suehiro, T. Takeda, M. Lu, T. Sekiguchi, N. Hirosaki, R. J. Xie, *J. Mater. Chem. C* **2015**, *3*, 3181.
[26] F. Iqbal, S. Kim, H. Kim, *Opt. Mater.* **2017**, *72*, 323.
[27] J. J. Fan, L. Zhou, Z. Cui, S. H. Chen, X. J. Fan, G. Q. Zhang, *J. Lumin.* **2020**, *219*, 116874.
[28] G. Mura, G. Cassanelli, F. Fantini, M. Vanzi, *Microelectron. Reliab.* **2008**, *48*, 1208.
[29] A. Zibold, M. Dammann, R. Schmidt, H. Konstanzer, M. Kunzer, *Microelectron. Reliab.* **2017**, *76*, 566.
[30] S. J. Clark, M. D. Segall, C. J. Pickard, P. J. Hasnip, M. J. Probert, K. Refson, M. C. Payne, *Z. Kristallogr. - Cryst. Mater.* **2005**, *220*, 567.
[31] A. M. Liu, W. X. Guan, X. D. Zhao, X. F. Ren, X. Y. Liang, L. G. Gao, Y. Q. Li, T. L. Ma, *Appl. Surf. Sci.* **2021**, *541*, 148570.
[32] J. P. Perdew, K. Burke, M. Ernzerhof, *Phys. Rev. Lett.* **1996**, *77*, 3865.
[33] S. Grimme, J. Antony, S. Ehrlich, H. Krieg, *J. Chem. Phys.* **2010**, *132*, 154104.
[34] H. J. Monkhorst, J. D. Pack, *Phys Rev. B* **1976**, *13*, 5188.
[35] Y. Zou, X. Y. Guo, X. Q. Bian, Y. F. Zhang, W. Lin, S. P. Huang, Z. F. Chen, K. N. Ding, *Appl. Surf. Sci.* **2022**, *592*, 153233.
[36] T. A. Halgren, W. N. Lipscomb, *Chem. Phys. Lett.* **1977**, *49*, 225.
[37] Z. Wang, B. Shen, F. Dong, S. Wang, W. S. Su, *Phys. Chem. Chem. Phys.* **2015**, *17*, 15065.
[38] M. Mikami, K. Uheda, N. Kijima, *Phys. Status Solidi A.* **2006**, *203*, 2705.
[39] S. Jang, J. Im, B. K. Bang, C. H. Kim, H. Chang, K. J. Kong, *RSC Adv.* **2015**, *5*, 39319.
[40] J. C. Dobson, A. Hinchliffe, *J. Mol. Struct.* **1975**, *27*, 161.